



## OPEN ACCESS

## EDITED BY

Muhammad Asif,  
Wuhan Institute of Technology, China

## REVIEWED BY

Tieqiao Chen,  
Hainan University, China  
Mazhar Ul-Islam,  
Dhofar University, Oman  
Mudasir Nazar,  
Jiangsu University, China

## \*CORRESPONDENCE

Lan Yu,  
yulan000@hotmail.com

## SPECIALTY SECTION

This article was submitted to  
Electrochemistry,  
a section of the journal  
Frontiers in Chemistry

RECEIVED 19 October 2022

ACCEPTED 21 November 2022

PUBLISHED 08 December 2022

## CITATION

Ren L, Zhang X, Du X, Wang J and Yu L  
(2022), Ordered phase transformation  
and Cu doping effects in room-  
temperature  
ferromagnetic  $\text{Sr}_3\text{YCo}_4\text{O}_{10.5+\delta}$ .  
*Front. Chem.* 10:1073946.  
doi: 10.3389/fchem.2022.1073946

## COPYRIGHT

© 2022 Ren, Zhang, Du, Wang and Yu.  
This is an open-access article  
distributed under the terms of the  
[Creative Commons Attribution License  
\(CC BY\)](https://creativecommons.org/licenses/by/4.0/). The use, distribution or  
reproduction in other forums is  
permitted, provided the original  
author(s) and the copyright owner(s) are  
credited and that the original  
publication in this journal is cited, in  
accordance with accepted academic  
practice. No use, distribution or  
reproduction is permitted which does  
not comply with these terms.

# Ordered phase transformation and Cu doping effects in room-temperature ferromagnetic $\text{Sr}_3\text{YCo}_4\text{O}_{10.5+\delta}$

Lingqi Ren<sup>1</sup>, Xiaodong Zhang<sup>1</sup>, Xiaoli Du<sup>1</sup>, Jianlu Wang<sup>2</sup> and  
Lan Yu<sup>1\*</sup>

<sup>1</sup>Faculty of Materials Science and Engineering, Kunming University of Science and Technology, Kunming, China, <sup>2</sup>State Key Laboratory of Infrared Physics, Shanghai Institute of Technical Physics, Chinese Academy of Sciences, Shanghai, China

$\text{Sr}_3\text{YCo}_4\text{O}_{10.5+\delta}$  (314-SYCO), with an unusual ordered structure and a high Curie temperature ( $T_c \approx 335$  K), is attracting increasing attention. Herein, to improve the electrical performance of 314-SYCO, Cu-doped  $\text{Sr}_3\text{YCo}_{4-x}\text{Cu}_x\text{O}_{10.5+\delta}$  ( $x = 0-0.8$ ) ceramics were prepared using a solid-state reaction method. Systematic research was conducted on both the ordered phase transformation and the effects of Cu doping on the microstructure, electrical transport characteristics, and magnetic properties. For  $x = 0-0.4$ , the (103) and (215) planes were observed and combined with Rietveld refinement results for the X-ray diffraction data, confirming the formation of ordered tetragonal  $\text{Sr}_3\text{YCo}_{4-x}\text{Cu}_x\text{O}_{10.5+\delta}$ . This phase was formed with a mass gain of  $\sim 0.8\%$  and heat released at  $\sim 1,042^\circ\text{C}$ . With increasing Cu content, the concentration of hole carriers also increased, leading to a substantial reduction in electrical resistivity. The electrical resistivity decreased by 92–99% at 300 K. The polycrystalline materials have semiconducting behaviour with a three-dimensional Mott variable-range hopping mechanism. For the magnetic properties, a Hopkinson peak was observed at 319 K, and the  $T_c$  was approximately 321 K for  $x = 0$ . The magnetisation and  $T_c$  decreased with increasing Cu content, and a G-type antiferromagnetic-to-ferromagnetic phase transition occurred due to the spin state change for some  $\text{Co}^{3+}$  ions from high/intermediate spin to low/intermediate spin. These results lay the groundwork for refinement of the sintering procedure and doping parameters to enhance the performance of 314-SYCO in the context of current applications such as microwave absorbers and solid oxide fuel cell cathodes.

## KEYWORDS

ordered phase transformation, electrical transport, room-temperature ferromagnetism, ceramics, Cu content

## 1 Introduction

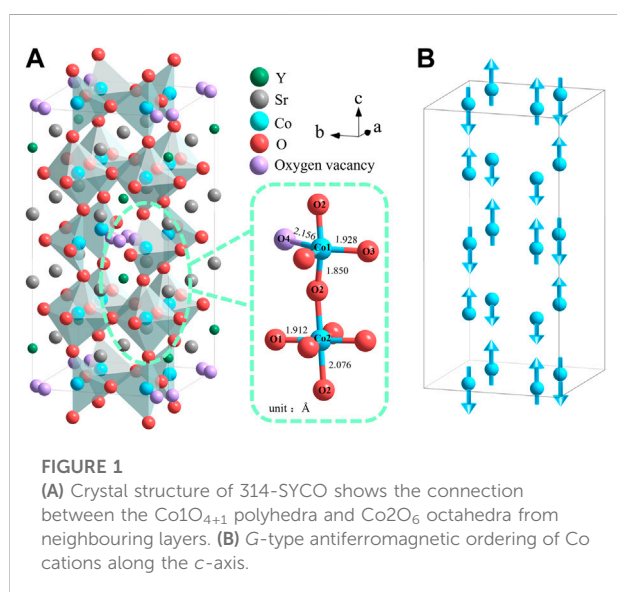
The oxygen-deficient perovskite  $\text{Sr}_3\text{YCo}_4\text{O}_{10.5+\delta}$  (314-SYCO) with an ordered tetragonal structure has potential applications in microwave absorbing materials, solid oxide fuel cells, and other fields owing to its room-temperature ferromagnetism (Goloso<sup>va</sup> et al., 2009; Marik et al., 2018; Istomin et al., 2003), orbital and charge ordering (Khalyavin et al., 2011; Sheptyakov et al., 2009; Kishida et al., 2016), high electronic conductivity, and excellent activity for the oxygen-reduction reaction (Li et al., 2011; Lalan et al., 2019). The A-site ordered (AO) and oxygen vacancy ordered (OO) tetragonal superstructure of 314-SYCO is composed of alternating octahedral  $\text{CoO}_6$  layers and tetrahedral  $\text{CoO}_{4.25+\delta}$  layers stacked along the *c*-axis. The A-site cations are arranged as  $-\text{Sr}-\text{Y}-\text{Y}-\text{Sr}-$  units along the *c*-axis, and the  $\text{Sr}^{2+}:\text{Y}^{3+}$  ratio is 3:1 in the *ab*-plane. The oxygen vacancies of the  $\text{CoO}_{4.25+\delta}$  layer are arranged in a zigzag pattern in the *bc*-plane (Khalyavin et al., 2011). For  $\delta = -0.26-0.3$ , 314-SYCO usually has an AO/OO tetragonal superstructure, as illustrated in Figure 1A (Istomin et al., 2003; Fukushima et al., 2009). Moreover, the basic magnetic structure of 314-SYCO is a G-type antiferromagnet, as illustrated in Figure 1B (Sheptyakov et al., 2009). The magnetic properties are mainly derived from oxygen ordering at oxygen-vacancy sites (Kobayashi et al., 2005; Fukushima et al., 2008; Fukushima et al., 2009).

The 314-SYCO material has a complex and interesting phase-transition process. Hu et al. (Hu et al., 2017) observed an exothermic peak at 963°C in differential scanning calorimetry (DSC) curves, corresponding to the crystallisation of 314-SYCO. In addition, a weight loss at 400°C in the thermogravimetric (TG) curves of 314-SYCO samples in oxygen, air, and helium atmospheres were observed due to the removal of O4 (the

Co1–O4 distance is the longest, as illustrated in Figure 1). At approximately 1,000°C in a helium atmosphere, the oxygen content in polycrystals that had lost most of their O4 was close to 10 ( $\text{Sr}_3\text{YCo}_4\text{O}_{10}$ ), resulting in a brownmillerite-type structure (Istomin et al., 2003). However, there are limited reports on the phase transition of 314-SYCO during its synthesis.

The phase structure, ordering, and physical properties of 314-SYCO could be modulated by Co-site doping. With increased Fe doping,  $\text{Sr}_{0.75}\text{Y}_{0.25}\text{Co}_{1-x}\text{Fe}_x\text{O}_{2.625+\delta}$  changes from an ordered tetragonal structure to a disordered cubic structure, while  $\text{Sr}_{0.75}\text{Y}_{0.25}\text{Co}_{1-x}\text{Ga}_x\text{O}_{2.625+\delta}$  has a tetragonal superstructure with decreased magnetic order at  $x = 0.25$  (Lindberg et al., 2006). In the  $\text{CoO}_6$  layer and/or antiferromagnetic  $\text{CoO}_{4.25}$  layer,  $\text{Ga}^{3+}$  ions both replace the high-spin-state  $\text{Co}^{3+}$  ions and increase the saturation magnetisation of Co ions. Further, it was shown that both the thermal expansion coefficient and conductivity of  $\text{Sr}_3\text{YCo}_{4-x}\text{Fe}_x\text{O}_{10.5+y}$  decrease at 1173 K (Istomin et al., 2008). According to previous studies, intermediate-spin state  $\text{Co}^{3+}$  ions get preferentially replaced by  $\text{Al}^{3+}$  ions in the ferrimagnetic  $\text{CoO}_6$  layer, which lowers the  $\text{Sr}_{3.1}\text{Y}_{0.9}\text{Co}_4\text{O}_{10.5}$  saturation magnetisation (Tsuruta et al., 2020). The addition of  $\text{Al}^{3+}$  disrupts the oxygen-ordering superstructure, which further inhibits the ferromagnetism of 314-SYCO at room temperature (Rajan and Subodh, 2020). As Cu has a similar ionic radius to Co, Cu doping at the Co site can directly increase carrier concentration. Therefore, the electrical properties of 314-SYCO can be significantly improved by substituting Co with Cu. In addition, CuO, as a sintering agent, increases the content of the liquid phase during sintering, thus improving the sintering quality. Our research group first proposed that Cu doping can reduce the resistivity of 314-SYCO (Du et al., 2014). However, a thorough investigation of the effects of Cu doping on the electromagnetic characteristics of polycrystalline 314-SYCO has not yet been conducted. The oxygen-deficient perovskite 314-SYCO has been proven to be useful as a microwave absorber or as a cathode for solid oxide fuel cells due to its high electronic conductivity and excellent activity for oxygen reduction reactions (Li et al., 2011; Lalan et al., 2019). Moreover, low electrical resistivity is an important physical parameter for microwave absorbers or cathodes for solid oxide fuel cells.

Here, the ordered phase transformation of 314-SYCO is reported for the first time. The microstructure, electrical transport, and magnetic properties of  $\text{Sr}_3\text{YCo}_{4-x}\text{Cu}_x\text{O}_{10.5+\delta}$  ( $x = 0, 0.2, 0.4$ ) were investigated in detail. For  $x = 0-0.4$ , the ordered tetragonal  $\text{Sr}_3\text{YCo}_{4-x}\text{Cu}_x\text{O}_{10.5+\delta}$  phase was formed. The key step in the formation of the ordered tetragonal phase is an exothermic reaction at  $\sim 1,042^\circ\text{C}$  and an oxygen mass gain of  $\sim 0.8\%$ . With increasing Cu content, the electrical resistivity decreases greatly, and the polycrystalline material shows the three-dimensional Mott variable-range hopping mechanism typical of a semiconductor. Additionally, a G-type antiferromagnetic-to-ferromagnetic phase transition occurs due to a reduction in the spin state of some  $\text{Co}^{3+}$  ions.



## 2 Material and methods

### 2.1 Materials and synthesis

Using a solid-state reaction technique,  $\text{Sr}_3\text{YCo}_{4-x}\text{Cu}_x\text{O}_{10.5+\delta}$  ( $x = 0, 0.2, 0.4, 0.6,$  and  $0.8$ ) was made polycrystalline. The raw materials were  $\text{SrCO}_3$  (99.95%),  $\text{Y}_2\text{O}_3$  (99.9%),  $\text{Co}_3\text{O}_4$  (99.9%), and  $\text{CuO}$  (99%). All starting materials were purchased from Shanghai Aladdin Biochemical Technology Co., Ltd. (Shanghai, China). Stoichiometric amounts of the starting reagents were weighed (Sr: Y: Co: Cu = 3:1: 4- $x$ :  $x$ ) and homogeneously mixed in an agate mortar for at least 120 min. Following this, the powdered mixture was pressed into disc-shaped tablets (4 MPa/5 min +5 MPa/5 min) with a diameter of 20 mm and height of 3.0–3.5 mm, which were sintered in air at 1,100°C for 24 h.

### 2.2 Characterization of samples

The phase transitions during the sintering of the  $\text{Sr}_3\text{YCo}_{4-x}\text{Cu}_x\text{O}_{10.5+\delta}$  raw ingredients were investigated using TG-DSC (STA449F3, Netzsch, Selb, Germany) from 25 to 1,100°C at a heating rate of  $\sim 10^\circ\text{C}/\text{min}$ ; the ingredient quantities were 7.5–9.5 mg. The phase structure of the sintered samples was identified using X-ray diffraction (XRD; Ultima IV, Rigaku Corporation, Tokyo, Japan;  $\text{CuK}\alpha$  radiation with wavelength  $\lambda = 1.5406 \text{ \AA}$ , step size of  $0.02^\circ$ ) through  $\theta$ - $2\theta$  scans (40 kV, 40 mA, scan range of  $10$ – $100^\circ$ , scan rate of  $4^\circ/\text{min}$ ) and slow scans ( $40 \text{ kV}$ ,  $40 \text{ mA}$ , scan ranges of  $20$ – $21^\circ$ ,  $38.5$ – $39.5^\circ$ , or  $46.5$ – $48^\circ$ , scan rate of  $0.4^\circ/\text{min}$ ). High-resolution transmission electron microscopy (HRTEM; Tecnai G2 F30 S-TWIN, FEI Company, Oregon, United States) and fast Fourier transform (FFT) analyses were used to establish the crystal structure. To examine the morphologies and Cu ion distributions, scanning electron microscopy coupled with energy-dispersive spectrometry (SEM-EDS; XL30ESEM, Philips, Amsterdam, Netherlands) was used. The sample density was measured using Archimedes' method. X-ray photoemission spectroscopy (XPS) was conducted on an electron spectrometer (PHI5000 VersaProbe III, ULVAC-PHI, Inc., Kanagawa, Japan) with a monochromatic Al K $\alpha$  irradiation source. Using a four-probe method, resistivity-temperature ( $\rho$ - $T$ ) curves were produced for the temperature range of 75–300 K. Seebeck coefficient-temperature ( $S$ - $T$ ) curves were recorded using a Seebeck measurement device (LSR-3/1,000, Linseis Messgeräte GmbH, Selb, Germany) in the temperature range of 300–1100 K. Using a superconducting quantum interference device (MPMS-XL, Quantum Design, Inc., California, United States) with a magnetic field of  $\sim 1 \text{ T}$  and a temperature range of 4–380 K, magnetisation-temperature ( $M$ - $T$ ) curves were measured.

## 3 Results and discussion

Figure 2 shows the XRD patterns of the polycrystalline  $\text{Sr}_3\text{YCo}_{4-x}\text{Cu}_x\text{O}_{10.5+\delta}$  ( $x = 0$ – $0.8$ ) sintered at 1,100°C for 24 h. For  $x = 0$ – $0.4$ , all diffraction peaks were indexed to the tetragonal superstructure (PDF#54–0,234), i.e.,  $I4/mmm$ . As the Cu doping content increased, the diffraction peaks of the samples shifted toward a lower angle, indicating an increase in the lattice constant due to the partial replacement of  $\text{Co}^{3+/4+}$  ( $0.61/0.53 \text{ \AA}$ ) by  $\text{Cu}^{2+}$  ( $0.73 \text{ \AA}$ ) (Hsieh and Fung, 2008; Zhao et al., 2010). Figures 2A,B show the presence of (008)(400), (228)(424), and (408)(440) split peaks. Both sets of spectra indicate  $a = b \neq 1/2c$ , which is characteristic of a tetragonal structure (Hu et al., 2017). The peaks of (103) and (215) in Figures 2C,D imply that  $\text{Sr}_3\text{YCo}_{4-x}\text{Cu}_x\text{O}_{10.5+\delta}$  polycrystals had an ordered lattice, consistent with the ordered tetragonal phase extinction law ( $h, k, l \neq 2n$ ) (Kobayashi et al., 2005). Figures 2E–G show that the experimentally measured XRD diffraction peaks exhibit a high degree of overlap with the feasibility of Rietveld refinement, indicating that the samples from  $x = 0$  to  $0.4$  are pure ordered tetragonal phase. The final reliability factors for the recorded patterns are  $R_{wp} = 3.346\%$  and  $\chi^2 = 1.69$  for  $x = 0$ ,  $R_{wp} = 3.503\%$  and  $\chi^2 = 1.77$  for  $x = 0.2$ , and  $R_{wp} = 6.719\%$  and  $\chi^2 = 3.30$  for  $x = 0.4$ .

The average grain size in the direction of the vertical grain plane (204),  $D_{(204)}$ , was calculated using Scherrer equation  $D_{D(204)} = K\lambda/\beta \cos \theta$  (Vinila and Isac, 2022). Here,  $\beta$  is the full width at half maximum of the peak, and  $K = 0.89$ . Table 1 summarises the lattice constant, grain size, linear shrinkage, and density of  $\text{Sr}_3\text{YCo}_{4-x}\text{Cu}_x\text{O}_{10.5+\delta}$  ( $x = 0, 0.2,$  and  $0.4$ ) samples. The linear shrinkage ( $\Delta L/L_0$ , where  $\Delta L$  is the shortening value after sintering and  $L_0$  is the diameter of the sample before sintering) and bulk density ( $P$ ) significantly increased with increasing  $x$ . In Figures 2A,C,D, the (103) and (215) diffraction peaks are very small for  $x = 0.6$ – $0.8$ , suggesting that the ordered phase was either minimal or not present.

Figure 3A displays the HRTEM pictures together with their accompanying FFT diffraction spots, and Figure 3B illustrates how the crystal structure of the  $\text{Sr}_3\text{YCo}_{4-x}\text{Cu}_x\text{O}_{10.5+\delta}$  ( $x = 0.2$ ) samples correspond to the diffraction spots. The  $d$ -spacings of 0.539 and 0.424 nm are indexed to the (1 $\bar{1}$ 0) and ( $\bar{1}$ 0 $\bar{3}$ ) lattice planes, respectively. The FFT pattern (inset in Figure 3A) and Figure 3B show the diffraction spots corresponding to the (1 $\bar{1}$ 0), (0 $\bar{1}$ 3), and ( $\bar{1}$ 0 $\bar{3}$ ) planes along the [33 $\bar{1}$ ] orientation. The superlattice (103) diffraction surface confirms that the tetragonal  $\text{Sr}_3\text{YCo}_{4-x}\text{Cu}_x\text{O}_{10.5+\delta}$  polycrystalline structure has an ordered superstructure.

TG-DSC curves were measured to simulate the sintering of the raw ingredients to produce  $\text{Sr}_3\text{YCo}_{4-x}\text{Cu}_x\text{O}_{10.5+\delta}$  ( $x = 0$ – $0.8$ ). Figures 4A–E show three stages in all TG curves, i.e., approximately 25–680°C for stage I, 680–969°C for stage II, and 969–1,100°C for stage III. The curves were similar for all samples in stages I and II.

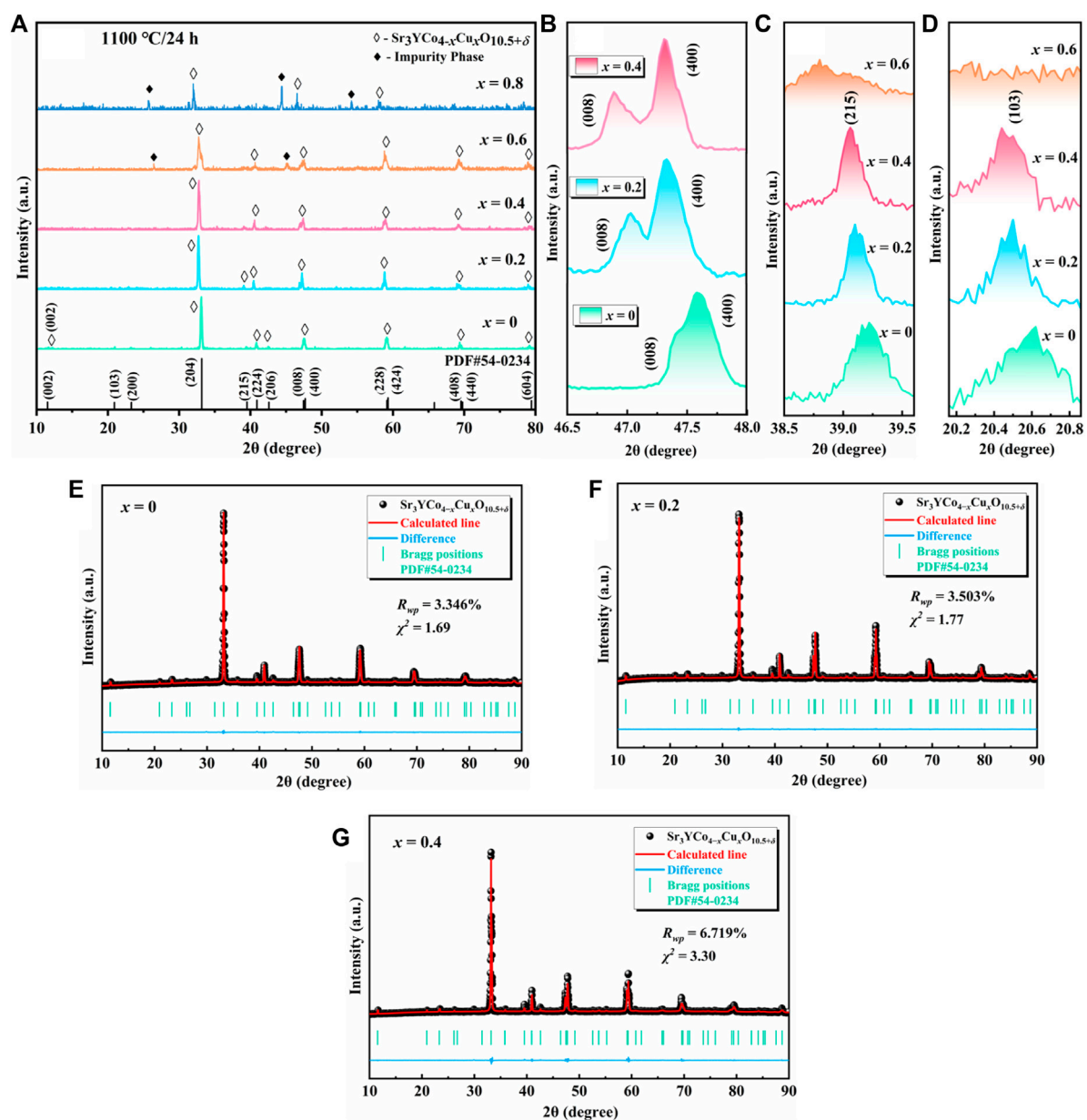
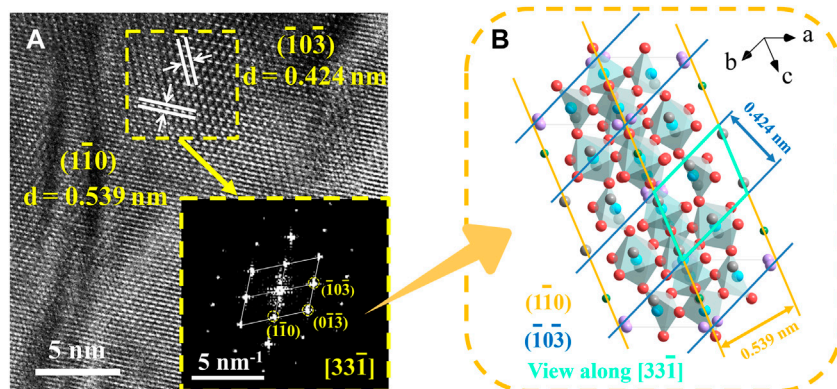


FIGURE 2

XRD patterns of  $\text{Sr}_3\text{YCo}_{4-x}\text{Cu}_x\text{O}_{10.5+\delta}$  ( $x = 0-0.8$ ) polycrystals sintered at  $1,100^\circ\text{C}$  for 24 h (A)  $x = 0-0.8$ ; slow scans ( $0.4^\circ/\text{min}$ ) of (B) (008)(400) split peak, (C) (103) peak, and (D) (215) peak. (E–G) XRD refinement results of  $\text{Sr}_3\text{YCo}_{4-x}\text{Cu}_x\text{O}_{10.5+\delta}$  ( $x = 0-0.4$ ).

TABLE 1 Crystal and physical properties of  $\text{Sr}_3\text{YCo}_{4-x}\text{Cu}_x\text{O}_{10.5+\delta}$  polycrystals sintered at  $1,100^\circ\text{C}$  for 24 h.

Sample	Lattice constant	Grain size	Linear shrinkage	Density	
	$a, b$ ( $\text{\AA}$ )			$c$ ( $\text{\AA}$ )	$D_{(204)}$ (nm)
$x = 0$	7.63	15.35	48.8	15.6	3.82
$x = 0.2$	7.67	15.41	54.5	20.5	4.90
$x = 0.4$	7.70	15.43	59.4	22.1	5.08

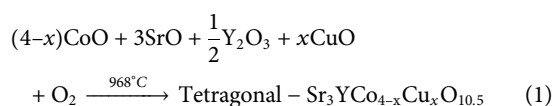


**FIGURE 3**

(A) HRTEM image of  $\text{Sr}_3\text{YCo}_{4-x}\text{Cu}_x\text{O}_{10.5+\delta}$  polycrystals:  $x = 0.2$  (ordered tetrahedral). The inset shows the corresponding FFT pattern of  $\text{Sr}_3\text{YCo}_{4-x}\text{Cu}_x\text{O}_{10.5+\delta}$ . (B) Relationship between the FFT diffraction spots and the corresponding crystal structure.

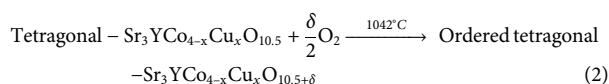
In stage I, the mass loss of all samples was in the range of 0.5–2.5% due to the dehydration of the raw materials. The mass loss was in the range of 12–15.6% in stage II. The endothermic peak at  $\sim 910^\circ\text{C}$  corresponds to the phase transition from orthorhombic to trigonal  $\text{SrCO}_3$  and the decomposition of  $\text{Co}_3\text{O}_4$  into  $\text{CoO}$  and  $\text{O}_2$  (Delorme et al., 2015). Trigonal  $\text{SrCO}_3$  is broken into  $\text{SrO}$  and  $\text{CO}_2$ , which produce the endothermic peak at  $\sim 933^\circ\text{C}$  (Ptáček et al., 2015).

As the temperature increased above  $946^\circ\text{C}$ , all TG curves showed further weight loss, indicating that  $\text{SrCO}_3$  continued to decompose. In the DSC curves, the exothermic peak at  $\sim 968^\circ\text{C}$  corresponds to the crystallisation of  $\text{Sr}_3\text{YCo}_{4-x}\text{Cu}_x\text{O}_{10.5}$ , because one of the four adjacent oxygen vacancies (Figure 1A) can be occupied easily ( $\text{O}_{10} \rightarrow \text{O}_{10.5}$ ) (Istomin et al., 2003; Rupasov et al., 2009), as indicated by Eq. 1.



For  $x = 0.2$ – $0.8$ , the weak endothermic peak observed at  $746$ – $811^\circ\text{C}$  may be related to a trace eutectic mixture formed by  $\text{CuO}$  and  $\text{SrCO}_3$ – $\text{Y}_2\text{O}_3$ – $\text{Co}_3\text{O}_4$  (Kingery and Narasimhan, 1959).

In stage III, the mass variation and thermal behaviour are significantly dependent on  $x$ . As shown in Figure 4F, the mass gain is 0.8–0.9% for  $x = 0$ – $0.4$ , while the DSC curves show a weak exothermic peak at approximately  $1,042^\circ\text{C}$ , corresponding to the uptake of oxygen ( $\delta$ ) (Eq. 2).



For  $x = 0.6$ – $0.8$ , the weak endothermic peak at  $978^\circ\text{C}$  may correspond to an impurity formed by heating. Despite a mass gain of 0.7–1%, the exothermic peaks related to the ordered phase

were not observed at  $\sim 1,042^\circ\text{C}$ . This observation is consistent with the XRD patterns in Figure 2, where the (103) and (215) peaks were not observed for  $x = 0.6$ . The lack of the ordered phase may be caused by excessive Cu doping, implying that the solid solubility of Cu is  $x = 0.4$ – $0.6$ .

Figure 5A shows photographs of polycrystalline  $\text{Sr}_3\text{YCo}_{4-x}\text{Cu}_x\text{O}_{10.5+\delta}$  sintered at  $1,100^\circ\text{C}$  for 24 h. For  $x = 0$ – $0.4$ , the surfaces are smooth and flat, and the volume drastically reduced with increasing  $x$  (i.e., enhanced sintering). For  $x = 0.6$ – $0.8$ , the corrosion of the samples with the crucible became increasingly severe as the dissolution exceeded the solid limit, and low-melting-point heterogeneous phases were produced. Cross-sectional SEM images of polycrystalline  $\text{Sr}_3\text{YCo}_{4-x}\text{Cu}_x\text{O}_{10.5+\delta}$  ( $x = 0$ – $0.4$ ) (Figures 5B–D) indicate the porous structures of these samples. With increasing  $x$ , an increased density is observed as a result of sintering, i.e., the pore volume reduced to form close grain connections (Figure 5E). These trends also align with the findings in Table 1. Figure 5F shows a surface SEM image of  $\text{Sr}_3\text{YCo}_{4-x}\text{Cu}_x\text{O}_{10.5+\delta}$  ( $x = 0.6$ ) polycrystalline material. The grain clusters are highlighted in blue and the lighter lines are the grain boundaries. According to EDS analysis, spot 2 (Figure 5H) has significantly higher Cu content than spot 1 (Figure 5G). Therefore, the grain clusters are thought to be a Cu-rich phase.

The XPS survey spectra of  $\text{Sr}_3\text{YCo}_{4-x}\text{Cu}_x\text{O}_{10.5+\delta}$  samples ( $x = 0, 0.2, \text{ and } 0.4$ ) are shown in Figure 6A, confirming the presence of elements in these samples; no other impurity elements were detected, demonstrating the high purity of the experimentally-produced polycrystals. The XPS Co elemental spectra for the samples ( $x = 0, 0.2, \text{ and } 0.4$ ) are presented in Figures 6B–D. In contrast with the  $\text{Co}^{3+}$  ion,  $\text{Co}^{4+}$  contains a more positive electrical charge and lower electron cloud density, thus the binding energy of 2p electrons should also be higher (LU

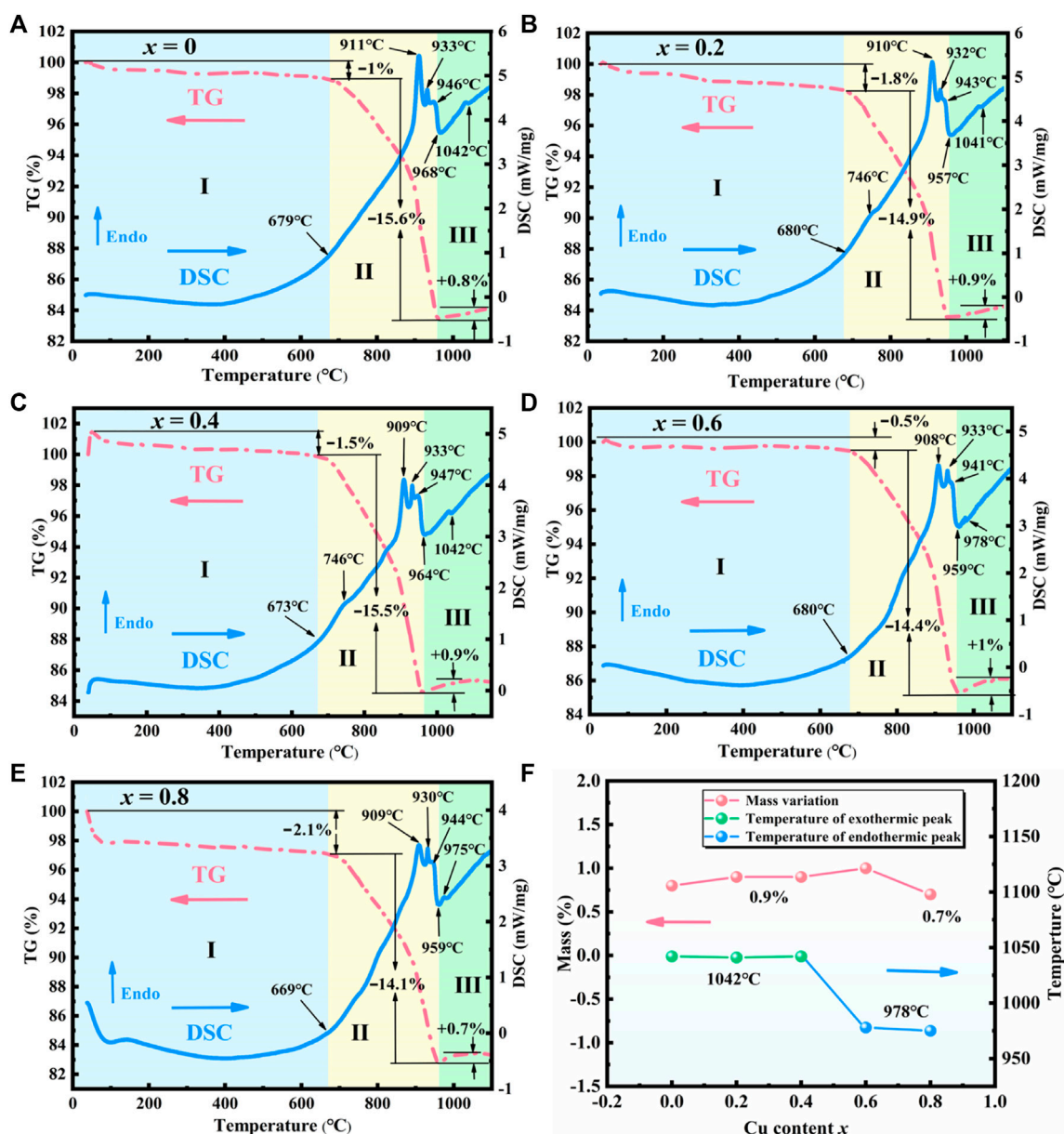
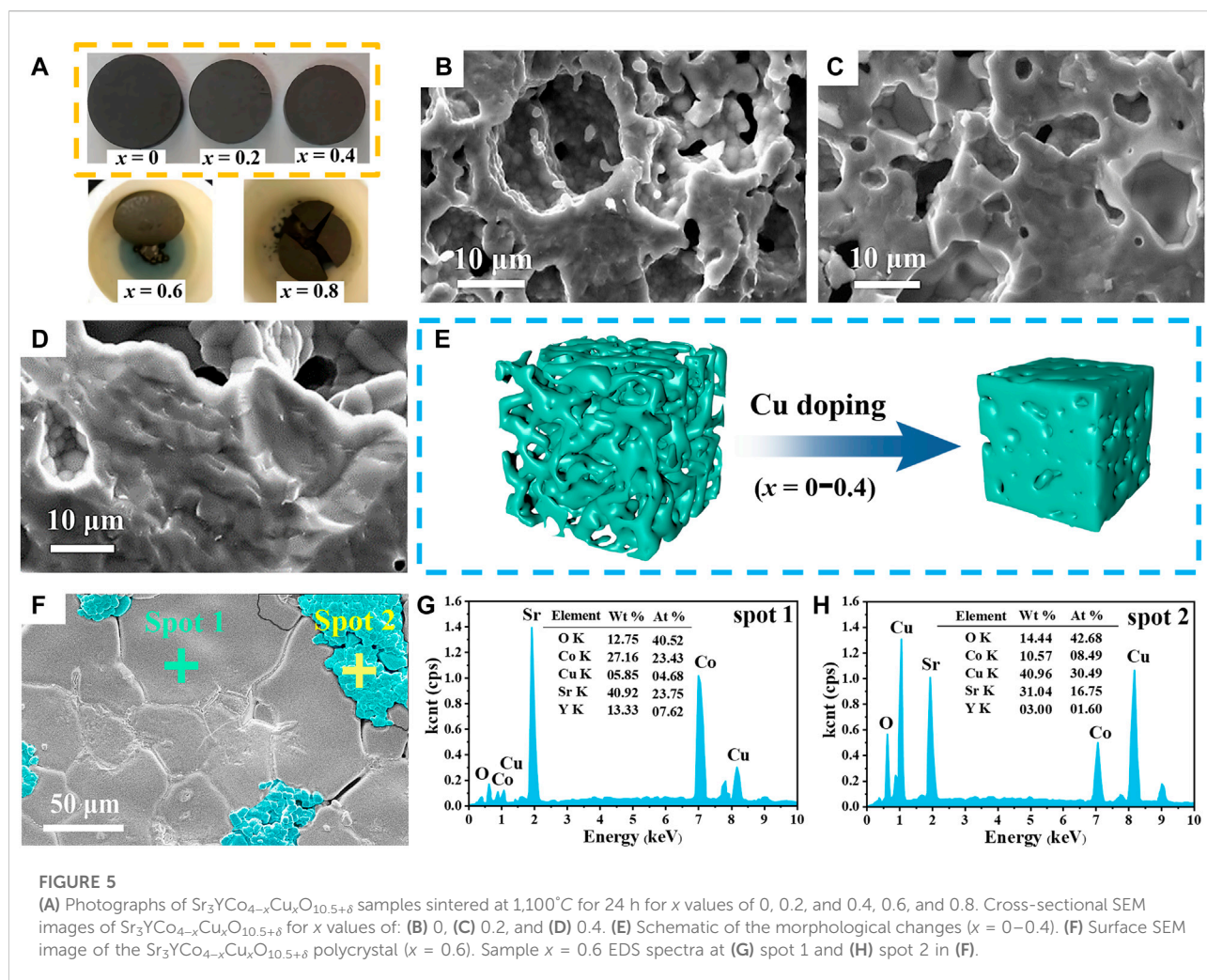


FIGURE 4

TG-DSC curves of the sintering ingredients of  $\text{Sr}_3\text{YCo}_{4-x}\text{Cu}_x\text{O}_{10.5+\delta}$  for  $x$  values of (A) 0, (B) 0.2, (C) 0.4, (D) 0.6, (E) 0.8. (F) Mass variation and thermal effects for  $x = 0-0.8$  in stage III.

et al., 2013). As a result,  $\text{Co}^{3+}$  ions have a lower binding energy than  $\text{Co}^{4+}$  ions. Therefore, the intensity peaks appearing at 779.77/794.74 eV for  $x = 0$ , 780.5/795.02 eV for  $x = 0.2$  and 779.68/794.65 eV for  $x = 0.4$  can be assigned to  $\text{Co}^{3+}$ , while the peaks of 782.18/797.15 eV for  $x = 0$ , 782.36/797.33 eV for  $x = 0.2$  and 781.81/796.78 eV for  $x = 0.4$  can be assigned to  $\text{Co}^{4+}$  ion. For each composition, the  $\text{Co}^{3+}/\text{Co}^{4+}$  ratio is determined by fitting the area under the curve. The  $\text{Co}^{3+}/\text{Co}^{4+}$  ratio for each composition is presented in Table 2. It was observed that the  $\text{Co}^{3+}$

content decreased significantly with the increase in the Cu doping amount. The XPS results confirm that the  $\text{Cu}^{2+}$  ions predominantly occupy  $\text{Co}^{3+}$  sites. In Figure 6E, the  $\text{Cu}^{2+}$  signal ( $\text{Cu}2p_{3/2}$  and  $\text{Cu}2p_{1/2}$  are 934.07 and 953.87 eV for  $x = 0.2$ , 933.49 and 953.29 eV for  $x = 0.4$ , respectively) and its satellite peak (936.0–946.0 eV) in the Cu 2p spectral range are obvious (Wu et al., 2018; Li et al., 2022). The results show that in  $\text{Sr}_3\text{YCo}_{4-x}\text{Cu}_x\text{O}_{10.5+\delta}$ , Cu ions exist in the oxidation state of +2 valence. Compared to the element Co, Cu 2p is relatively



weak. This phenomenon is consistent with its low element content.

As shown in **Figure 7A**, the resistivity-temperature ( $\rho$ - $T$ ) curves of polycrystalline  $\text{Sr}_3\text{YCo}_{4-x}\text{Cu}_x\text{O}_{10.5+\delta}$  ( $x = 0-0.6$ ) showed electrical transport characteristics typical of a semiconductor. The resistivity decreased significantly from  $x = 0$  to 0.4 and stabilised from  $x = 0.4$  to 0.6. **Figure 7B** shows that the room temperature resistivity at 300 K for  $x = 0.4$  and  $x = 0.6$  is  $0.0277203 \Omega \text{ cm}$  and  $0.0040672 \Omega \text{ cm}$ , respectively. Compared with the room temperature resistivity at  $x = 0$  of  $0.3403219 \Omega \text{ cm}$ , the resistivity decreased by 92–99% with Cu doping.

The  $\ln\rho$ - $T^{-1/(n+1)}$  curve was fitted using the Mott variable-range hopping model expressed in **Eq. 3** (Mott, 1969):

$$\rho = \rho_0 \cdot \exp(T_m/T)^{1/(n+1)} \quad (3)$$

Here,  $\rho_0$  is the initial electrical resistivity (constant),  $T_m$  is the characteristic temperature of the variable-range hopping

mechanism, and  $n = 2$  or  $n = 3$  is the dimension of the system. **Figure 7C** shows that when  $n = 3$ ,  $\ln\rho$ - $T^{-1/4}$  is almost linear for  $x = 0-0.04$ , indicating that a small number of  $\text{Co}^{4+}$  ions provide hole carriers (Terasaki et al., 2010), and hopping conduction occurs between  $\text{Co}^{4+}$  ions via a three-dimensional variable-range hopping mechanism. A deviation was found between the experimental and fitted curves for the  $x = 0.6$  sample, which may be caused by changes in the resistivity induced by impurity phases produced beyond the limit of solid solubility of Cu in the perovskite structure. When  $\text{Co}^{3+/4+}$  was replaced with  $\text{Cu}^{2+}$ , the concentration of hole carriers increased. In addition, the mobility of the hole carriers increased as the grain size and density of  $\text{Sr}_3\text{YCo}_{4-x}\text{Cu}_x\text{O}_{10.5+\delta}$  increased due to sintering.

The S- $T$  curves of  $\text{Sr}_3\text{YCo}_{4-x}\text{Cu}_x\text{O}_{10.5+\delta}$  ( $x = 0-0.4$ ) in **Figure 7D** indicate that the thermopower decreased with increasing temperature. The curves for  $x = 0$  and 0.2 are very similar, and the thermopower of the  $x = 0.4$  material was

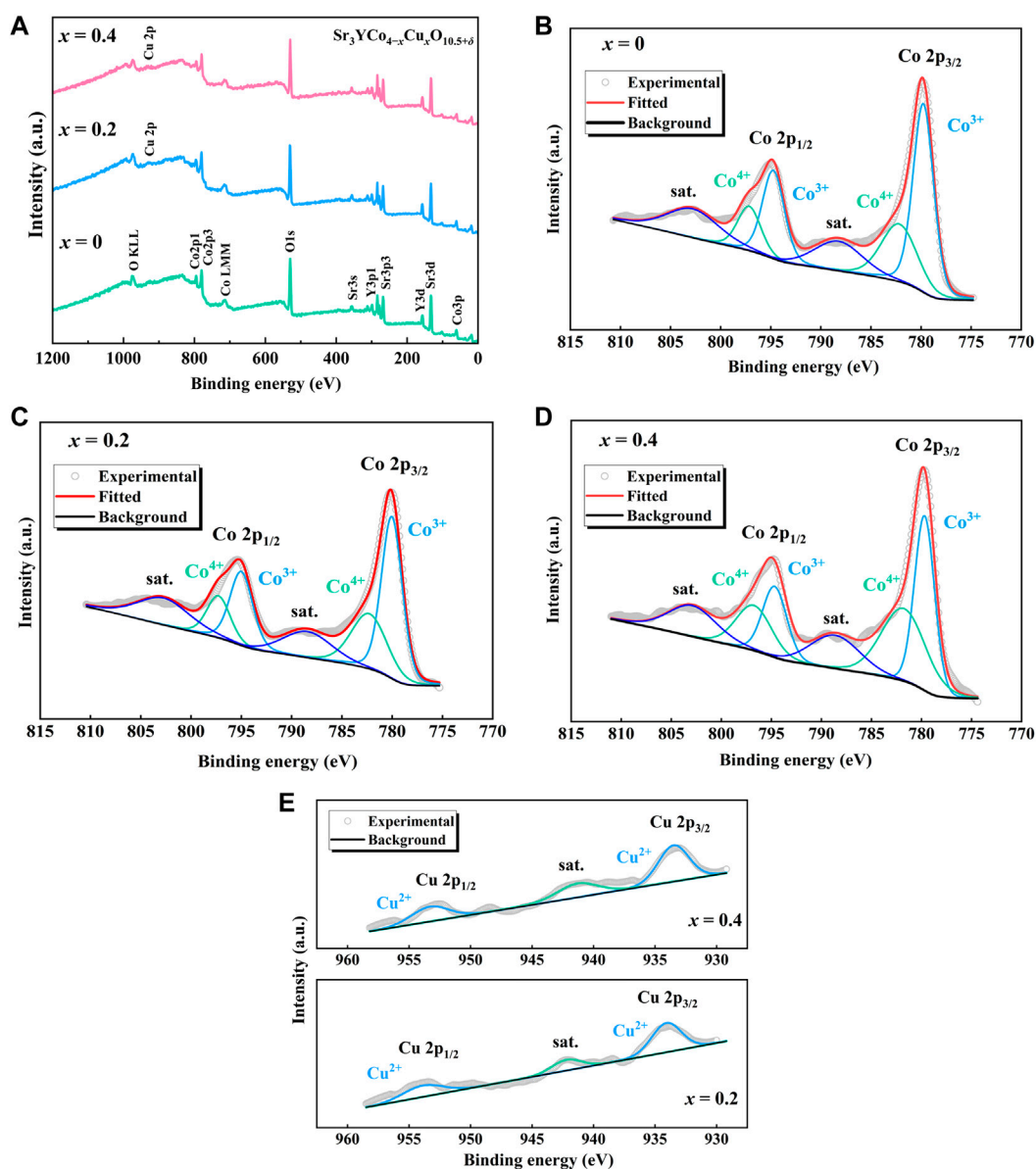


FIGURE 6

(A) Survey spectra of  $\text{Sr}_3\text{YCo}_{4-x}\text{Cu}_x\text{O}_{10.5+\delta}$  samples ( $x = 0, 0.2,$  and  $0.4$ ). (B–D) Co 2p XPS spectra of  $\text{Sr}_3\text{YCo}_{4-x}\text{Cu}_x\text{O}_{10.5+\delta}$  samples ( $x = 0, 0.2,$  and  $0.4$ ). (E) Cu 2p XPS spectra of  $\text{Sr}_3\text{YCo}_{4-x}\text{Cu}_x\text{O}_{10.5+\delta}$  samples ( $x = 0.2$  and  $0.4$ ).

TABLE 2  $\text{Co}^{3+}/\text{Co}^{4+}$  ion ratio in  $\text{Sr}_3\text{YCo}_{4-x}\text{Cu}_x\text{O}_{10.5+\delta}$  ( $x = 0, 0.2,$  and  $0.4$ ).

Compound	$\text{Sr}_3\text{YCo}_4\text{O}_{10.5+\delta}$	$\text{Sr}_3\text{YCo}_{3.8}\text{Cu}_{0.2}\text{O}_{10.5+\delta}$	$\text{Sr}_3\text{YCo}_{3.6}\text{Cu}_{0.4}\text{O}_{10.5+\delta}$
$\text{Co}^{3+}/\text{Co}^{4+}$ ratio	1.877	1.633	1.141

significantly lower due to the higher carrier concentration. In contrast, increasing the spin entropy of the  $\text{Co}^{3+}$  ions increases the thermopower (Yoshida et al., 2009).

The  $M-T$  and  $dM/dT-T$  curves of polycrystalline  $\text{Sr}_3\text{YCo}_{4-x}\text{Cu}_x\text{O}_{10.5+\delta}$  ( $x = 0-0.4$ ) are shown in Figures 8A,B. For  $x = 0$ , the Hopkinson peak is observed at 319 K in the zero-

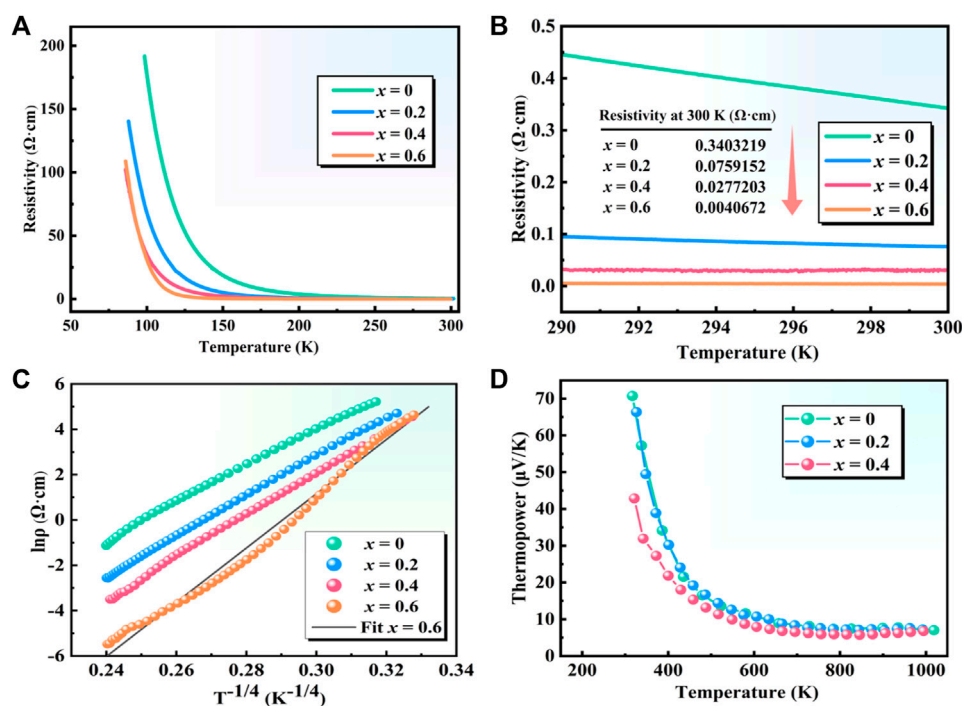


FIGURE 7

$\rho$ - $T$  curves of polycrystalline  $\text{Sr}_3\text{YCo}_{4-x}\text{Cu}_x\text{O}_{10.5+\delta}$  ( $x = 0-0.6$ ): (A) 50–300 K, (B) 290–300 K. This is a Kelvin temperature unit. (C)  $\ln\rho$ - $T^{-1/4}$  and (D)  $S$ - $T$  curves of polycrystalline  $\text{Sr}_3\text{YCo}_{4-x}\text{Cu}_x\text{O}_{10.5+\delta}$  ( $x = 0-0.4$ ).

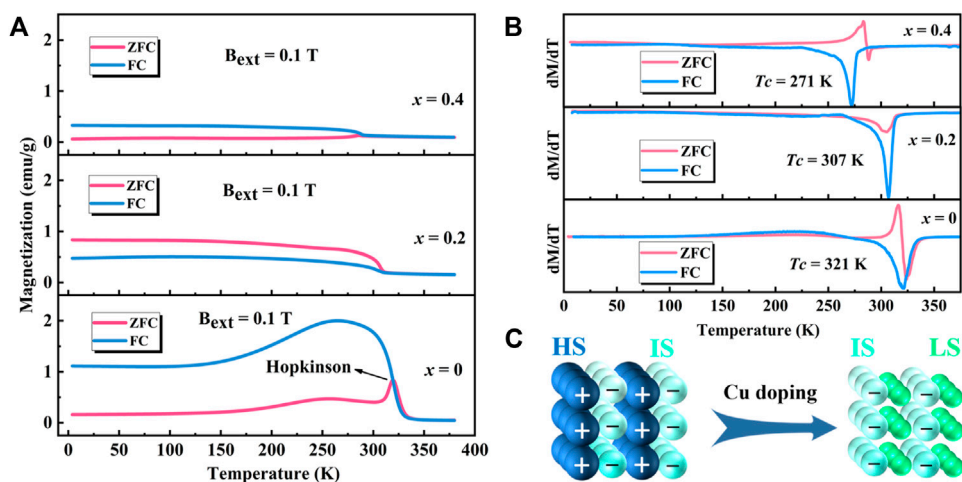


FIGURE 8

Magnetic properties of  $\text{Sr}_3\text{YCo}_{4-x}\text{Cu}_x\text{O}_{10.5+\delta}$  ( $x = 0-0.4$ ): (A)  $M$ - $T$ , (B)  $dM/dT$ - $T$  curves, and (C) spin states of  $\text{Co}^{3+}$  ions in  $\text{Sr}_3\text{YCo}_{4-x}\text{Cu}_x\text{O}_{10.5+\delta}$ .

field-cooling (ZFC) curve. Magnetic moments in the magnetic domains of materials are randomly distributed and frozen at low temperatures, and the net magnetic moments tend to be zero in

G-type antiferromagnetic phases (Sheptyakov et al., 2009; Troyanchuk et al., 2009; Troyanchuk et al., 2019). As the temperature increases, the magnetic moments rotate to align

along the direction of the external magnetic field, while the magnetic domain wall moves and the magnetic domain grows. When all magnetic moments are aligned in the same direction, the magnetic domain walls disappear, and the magnetisation reaches its maximum at 319 K. At  $T_c$ , thermal agitation causes magnetic moments to misalign, resulting in a ferromagnetic-paramagnetic second-order transition and a decrease in magnetisation. There is no resistance between the magnetic domain walls when the field-cooling (FC) curve is recorded, and the magnetic moments are aligned in the same direction under an external magnetic field. Therefore, the maximum magnetisation obtained for the FC curve was higher than that obtained for the ZFC curve. The FC curves had the highest peak at 267 K. As the temperature continues to decrease, a ferromagnetic-antiferromagnetic transition occurs, and a G-type antiferromagnetic phase is generated (Lindberg et al., 2006). The separation of the ZFC and FC curves at low temperature indicates that spin-glass state-like components may be present (Motohashi et al., 2005; Sutjahja et al., 2015; Guo et al., 2018; Srivastava et al., 2020).

For  $x = 0.2$ , the maximum magnetisation of the ZFC curve was found at 4 K, attributed to the chemical compressive stress induced by lattice distortion due to Cu doping. It allows most  $\text{Co}^{3+}$  ions to transit from a high/intermediate spin (HS/IS,  $t_{2g}^4 e_g^2 / t_{2g}^5 e_g^1$ ,  $S = 2/1$ ) to an intermediate/low spin (IS/LS,  $t_{2g}^5 e_g^1 / t_{2g}^6 e_g^0$ ,  $S = 1/0$ ), resulting in a decrease in magnetisation (Tsuruta et al., 2020). The  $\text{Co}^{3+}$  ions in the LS state are nonmagnetic. At this point, the spin magnetic moments of the  $\text{Co}^{3+}$  ions in most regions are aligned in the same direction, as shown in Figure 8C, which is similar to the ferromagnetic structure. The  $T_c$  from the ZFC curves decreased from 320 K ( $x = 0$ ) to 307 K ( $x = 0.2$ ) and 288 K ( $x = 0.4$ ), which is related to the decrease in the spin state of  $\text{Co}^{3+}$  ions, leading to a decrease in magnetisation and weakening of the magnetic interaction. Moreover, in conjunction with the XPS results, the doping of Cu ions instead of Co ions led to a reduction in  $\text{Co}^{3+}$  ion content, which has a direct effect on the reduction of the magnetisation intensity of the sample.

## 4 Conclusion

A conventional solid-state reaction method was used to synthesise polycrystalline  $\text{Sr}_3\text{YCo}_{4-x}\text{Cu}_x\text{O}_{10.5+\delta}$  ( $x = 0-0.8$ ). An ordered tetragonal phase and ordering phase transformations due to oxygen uptake above 1,000°C were observed for  $x = 0-0.4$  for the first time. An ordered tetragonal phase and ordering phase transformation due to oxygen uptake above 1,000°C were observed for  $x = 0-0.4$  for the first time. A study of the phase-transformations process during heating

provides a research reference for optimising the conditions of the material synthesis process, such as sintering temperature and holding time. Cu doping was observed to significantly reduce the electrical resistivity, and the three-dimensional Mott variable-range hopping conduction mechanism of polycrystalline  $\text{Sr}_3\text{YCo}_{4-x}\text{Cu}_x\text{O}_{10.5+\delta}$  was explored. We also found that Cu doping reduced both the spin state and content of  $\text{Co}^{3+}$  ions, thereby inhibiting the room temperature ferromagnetism of 314-SYCO and providing a reference for doping to modulate the properties of oxygen-deficient perovskites.

## Data availability statement

The original contributions presented in the study are included in the article/supplementary material, further inquiries can be directed to the corresponding author.

## Author contributions

Investigation, Data curation, Writing-original draft, Writing—review and editing, LR; Discussion, XZ, XD, and JW; Conceptualization, Investigation, Writing—review and editing, Supervision, Resources, LY.

## Funding

This work was supported by the National Natural Science Foundation of China (grant numbers 51462017 and 51962017).

## Conflict of interest

The authors declare that the research was conducted in the absence of any commercial or financial relationships that could be construed as a potential conflict of interest.

## Publisher's note

All claims expressed in this article are solely those of the authors and do not necessarily represent those of their affiliated organizations, or those of the publisher, the editors and the reviewers. Any product that may be evaluated in this article, or claim that may be made by its manufacturer, is not guaranteed or endorsed by the publisher.

## References

- Delorme, F., Diaz-Chao, P., Guilmeau, E., and Giovannelli, F. (2015). Thermoelectric properties of  $\text{Ca}_3\text{Co}_4\text{O}_9\text{-Co}_3\text{O}_4$  composites. *Ceram. Int.* 41 (8), 10038–10043. doi:10.1016/j.ceramint.2015.04.091
- Du, X. L., Yu, L., Zhang, B., Song, S. J., and Li, G. F. (2014). Effects of Cu doping on the microstructure and electrical properties of  $\text{Sr}_3\text{YCo}_4\text{O}_{10.5+\delta}$  polycrystalline. *Adv. Mat. Res.* 934, 80–85. doi:10.4028/www.scientific.net/AMR.934.80
- Fukushima, S., Sato, T., Akahoshi, D., and Kuwahara, H. (2009). Order-disorder effect of A-site and oxygen-vacancy on magnetic and transport properties of  $\text{Y}_{1-x}\text{Sr}_{3/4}\text{CoO}_{3-\delta}$ . *J. Phys. Soc. Jpn.* 78, 064706–6. doi:10.1143/JPSJ.78.064706
- Fukushima, S., Sato, T., Akahoshi, D., and Kuwahara, H. (2008). Comparative study of ordered and disordered  $\text{Y}_{1-x}\text{Sr}_x\text{CoO}_{3-\delta}$ . *J. Appl. Phys.* 103, 07F705–4. doi:10.1063/1.2830615
- Golosova, N. O., Kozlenko, D. P., Dubrovinsky, L. S., Drozhzhin, O. A., Istomin, S. Y., and Savenko, B. N. (2009). Spin state and magnetic transformations in  $\text{Sr}_{0.7}\text{Y}_{0.3}\text{CoO}_{2.62}$  at high pressures. *Phys. Rev. B* 79, 104431–104437. doi:10.1103/PhysRevB.79.104431
- Guo, X., Tong, P., Lin, J., Yang, C., Zhang, K., and Lin, S. (2018). Effects of Cr substitution on negative thermal expansion and magnetic properties of antiperovskite  $\text{Ga}_{1-x}\text{Cr}_x\text{N}_{0.83}\text{Mn}_3$  compounds. *Front. Chem.* 6, 75. doi:10.3389/fchem.2018.00075
- Hsieh, C. Y., and Fung, K. Z. (2008). Effect of divalent dopants on defect structure and electrical properties of  $\text{Bi}_2\text{WO}_6$ . *J. Phys. Chem. Solids* 69, 302–306. doi:10.1016/j.jpcs.2007.07.106
- Hu, J. L., Yu, L., Du, X. L., and Song, S. J. (2017). Preparation and properties of room-temperature ferromagnet  $\text{Sr}_3\text{YCo}_4\text{O}_{10.5+\delta}$  polycrystals. *J. Synth. Cryst.* 46, 238–242. (Chinese). doi:10.3969/j.issn.1000-985X.2017.02.008
- Istomin, S. Y., Drozhzhin, O. A., Napolsky, P. S., Putilin, S. N., Gippius, A. A., and Antipov, E. V. (2008). Thermal expansion behavior and high-temperature transport properties of  $\text{Sr}_3\text{YCo}_{4-x}\text{Fe}_x\text{O}_{10.5+y}$ ,  $x=0.0, 1.0, 2.0$  and  $3.0$ . *Solid State Ionics* 179, 1054–1057. doi:10.1016/j.ssi.2008.01.017
- Istomin, S. Y., Grins, J., Svensson, G., Drozhzhin, O. A., Kozhevnikov, V. L., Antipov, E. V., et al. (2003). Crystal structure of the novel complex cobalt oxide  $\text{Sr}_{0.7}\text{Y}_{0.3}\text{CoO}_{2.62}$ . *Chem. Mat.* 15, 4012–4020. doi:10.1021/cm034263e
- Khalyavin, D. D., Chapon, L. C., Suard, E., Parker, J. E., Thompson, S. P., and Yaremchenko, A. A. (2011). Complex room-temperature ferromagnetism induced by zigzag stripes of oxygen vacancies in  $\text{Sr}_3\text{YCo}_4\text{O}_{10+\delta}$ . *Phys. Rev. B* 83, 140403–140411. doi:10.1103/PhysRevB.83.140403
- Kingery, W. D., and Narasimhan, M. D. (1959). Densification during sintering in the presence of a liquid phase. II. Experimental. *J. Appl. Phys.* 30, 307–310. doi:10.1063/1.1735156
- Kishida, T., Kapetanakis, M. D., Yan, J. Q., Sales, B. C., Pantelides, S. T., and Pennycook, S. J. (2016). The origin of magnetic ordering in  $\text{Sr}_3\text{YCo}_4\text{O}_{10+x}$ . *Microsc. Microanal.* 22, 1394–1395. doi:10.1017/S1431927616007819
- Kobayashi, W., Ishiwata, S., Terasaki, I., Takano, M., Grigoraviciute, I., and Yamauchi, H. (2005). Room-temperature ferromagnetism in  $\text{Sr}_{1-x}\text{Y}_x\text{CoO}_{3-\delta}$  ( $0.2 \leq x \leq 0.25$ ). *Phys. Rev. B* 72, 1–5. doi:10.1103/PhysRevB.72.104408
- Lalan, V., Puthiyedath Narayanan, A., Surendran, K. P., and Ganesanpotti, S. (2019). Room-temperature ferromagnetic  $\text{Sr}_3\text{YCo}_4\text{O}_{10+\delta}$  and carbon black-reinforced polyvinylidene fluoride composites toward high-performance electromagnetic interference shielding. *ACS Omega* 4, 8196–8206. doi:10.1021/acsomega.9b00454
- Li, W., Liang, K., Wang, J., Wen, J., Shi, J., and Zhang, Z. (2022). Effects of Cu doping on electrochemical NOx removal by  $\text{La}_{0.8}\text{Sr}_{0.2}\text{MnO}_3$  perovskites. *Environ. Res.* 210, 112955. doi:10.1016/j.envres.2022.112955
- Li, Y., Kim, Y. N., Cheng, J., Alonso, J. A., Hu, Z., and Chin, Y. Y. (2011). Oxygen-deficient perovskite  $\text{Sr}_{0.7}\text{Y}_{0.3}\text{CoO}_{2.65-\delta}$  as a cathode for intermediate-temperature solid oxide fuel cells. *Chem. Mat.* 23, 5037–5044. doi:10.1021/cm202542q
- Lindberg, F., Drozhzhin, O. A., Istomin, S. Y., Svensson, G., Kaynak, F. B., and Svedlindh, P. (2006). Synthesis and characterization of  $\text{Sr}_{0.75}\text{Y}_{0.25}\text{Co}_{1-x}\text{M}_x\text{O}_{2.625+\delta}$  ( $M=\text{Ga}, 0.125 \leq x \leq 0.500$  and  $M=\text{Fe}, 0.125 \leq x \leq 0.875$ ). *J. Solid State Chem.* 179, 1434–1444. doi:10.1016/j.jssc.2006.01.057
- Lu, Y., Chen, L., Lu, C., Ni, Y., and Xu, Z. (2013). Effects of oxygen defects on structure and properties of  $\text{Sm}_{0.5}\text{Sr}_{0.5}\text{CoO}_{3-\delta}$  annealed in different atmospheres. *J. Rare Earths* 31, 1183–1190. doi:10.1016/s1002-0721(12)60424-4
- Marik, S., Mohanty, P., Singh, D., and Singh, R. P. (2018). Moderate magnetic field induced large exchange bias effect in ferrimagnetic  $314\text{-Sr}_3\text{YCo}_4\text{O}_{10.5}$  material. *J. Phys. D. Appl. Phys.* 51 (6), 065006. doi:10.1088/1361-6463/aaa452
- Motohashi, T., Caignaert, V., Pralong, V., Hervieu, M., Maignan, A., and Raveau, B. (2005). Competition between ferromagnetism and spin glass: The key for large magnetoresistance in oxygen-deficient perovskites  $\text{SrCo}_{1-x}\text{M}_x\text{O}_{3-\delta}$  ( $M=\text{Nb}, \text{Ru}$ ). *Phys. Rev. B* 71, 214424. doi:10.1103/physrevb.71.214424
- Mott, N. F. (1969). Conduction in non-crystalline materials: III. Localized states in a pseudogap and near extremities of conduction and valence bands. *Philos. Mag.* 19, 835–852. doi:10.1080/14786436908216338
- Ptáček, P., Bartoničková, E., Švec, J., Opravil, T., Šoukal, F., and Frajkorová, F. (2015). The kinetics and mechanism of thermal decomposition of  $\text{SrCO}_3$  polymorphs. *Ceram. Int.* 41 (1), 115–126. doi:10.1016/j.ceramint.2014.08.043
- Rajan, A., and Subodh, G. (2020). Crystal structure, microstructure, and broadband electromagnetic response of  $\text{Al}^{3+}$ -substituted  $\text{Sr}_3\text{YCo}_4\text{O}_{10+\delta}$  double perovskites. *Ceram. Int.* 46 (16), 25683–25690. doi:10.1016/j.ceramint.2020.07.044
- Rupasov, D., Chronos, A., Parfitt, D., Kilner, A., Grimes, W., and Istomin, S.-Y. (2009). Oxygen diffusion in  $\text{Sr}_{0.75}\text{Y}_{0.25}\text{CoO}_{2.625}$ : A molecular dynamics study. *Phys. Rev. B* 79, 172102–172109. doi:10.1103/PhysRevB.79.172102
- Sheptyakov, D. V., Pomjakushin, V. Y., Drozhzhin, O. A., Istomin, S. Y., Antipov, E. V., and Bobrikov, I. A. (2009). Correlation of chemical coordination and magnetic ordering in  $\text{Sr}_3\text{YCo}_4\text{O}_{10.5+\delta}$  ( $\delta=0.02$  and  $0.26$ ). *Phys. Rev. B* 80, 024409. doi:10.1103/PhysRevB.80.024409
- Srivastava, A., Singh, A. K., Srivastava, O. N., Tewari, H. S., Masood, K. B., and Singh, J. (2020). Magnetic and dielectric properties of La and Ni Co-substituted  $\text{BiFeO}_3$  nanoceramics. *Front. Phys.* 8. doi:10.3389/fphys.2020.00282
- Sutjahja, I. M., Berthalita, F., Mustaqima, M., Nugroho, A. A., and Tjia, M. O. (2015). Effects of partial Co replacement by Fe in  $\text{Sr}_{0.775}\text{Y}_{0.225}\text{CoO}_{3-\delta}$  on its magnetic property, oxygen deficiency and crystal structure. *Mater. Pol.* 33, 579–587. doi:10.1515/msp-2015-0078
- Terasaki, I., Iwakawa, M., Nakano, T., Tsukuda, A., and Kobayashi, W. (2010). Novel thermoelectric properties of complex transition-metal oxides. *Dalton Trans.* 39, 1005–1011. doi:10.1039/b914661j
- Troyanchuk, I. O., Bushinsky, M. V., Tereshko, N. V., Lanovsky, R. A., Sikolenko, V. V., and Ritter, C. (2019). Ferromagnet-antiferromagnet transition in layered perovskites of  $\text{Sr}_3\text{YCo}_4\text{O}_{10.5}$  type. *Mat. Res. Express* 6, 026105. doi:10.1088/2053-1591/aaef21
- Troyanchuk, I. O., Karpinsky, D. V., Dobryanski, V. M., Chobot, A. N., Chobot, G. M., and Sazonov, A. P. (2009). Magnetic transformations in the  $\text{Sr}_{0.78}\text{Y}_{0.22}\text{Co}_{1-x}\text{Fe}_x\text{O}_{3-\gamma}$  system with a perovskite structure. *J. Exp. Theor. Phys.* 108, 428–434. doi:10.1134/S1063776109030078
- Tsuruta, A., Kawasaki, S., Mikami, M., Kinemuchi, Y., Masuda, Y., and Fujita, A. (2020). Co-substitution effect in room-temperature ferromagnetic oxide  $\text{Sr}_{3.1}\text{Y}_{0.9}\text{Co}_4\text{O}_{10.5}$ . *Mater. (Basel)* 13, 2301. doi:10.3390/ma13102301
- Vinila, V. S., and Isac, J. (2022). Synthesis and structural studies of superconducting perovskite  $\text{GdBa}_2\text{Ca}_3\text{Cu}_4\text{O}_{10.5+\delta}$  nanosystems. *Des. Fabr. Charact. Multifunct. Nanomater.*, 319–341. doi:10.1016/b978-0-12-820558-7.00022-4
- Wu, Y., Li, L., Chu, B., Yi, Y., Qin, Z., and Fan, M. (2018). Catalytic reduction of NO by CO over B-site partially substituted  $\text{LaM}_{0.25}\text{Co}_{0.75}\text{O}_3$  ( $M = \text{Cu}, \text{Mn}, \text{Fe}$ ) perovskite oxide catalysts: The correlation between physicochemical properties and catalytic performance. *Appl. Catal. A General* 568, 43–53. doi:10.1016/j.apcata.2018.09.022
- Yoshida, S., Kobayashi, W., Nakano, T., Terasaki, I., Matsubayashi, K., and Uwatoko, Y. (2009). Chemical and physical pressure effects on the magnetic and transport properties of the A-site ordered perovskite  $\text{Sr}_3\text{YCo}_4\text{O}_{10.5}$ . *J. Phys. Soc. Jpn.* 78, 094711–094715. doi:10.1143/JPSJ.78.094711
- Zhao, J., Chen, D. J., Shao, Z. P., and Liu, S. M. (2010). Effect of CuO additive on the sintering and performance of niobium-doped strontium cobaltite as oxygen separation membranes. *Sep. Purif. Technol.* 74, 28–37. doi:10.1016/j.seppur.2010.05.004